PNAS RESEARCH ARTICLE | CHEMISTRY

# Revealing the catalytic kinetics and dynamics of individual Pt atoms at the single-molecule level

Xiaodong Liu[a,b,c,d,1], Xin Ge[e,f,g,h,i,1], Jing Cao[a,b,c,1], Yi Xiao[a,b,c], Yan Wang[e,f,g,h,i], Wei Zhang[e,f,g,h,i,2], Ping Song[a,b,c,2], and Weilin Xu[a,b,c,2]

Edited by Alexis Bell, University of California, Berkeley, CA; received August 9, 2021; accepted January 31, 2022

**Due to the importance of single-atom catalysts (SAC), here, the catalysis of Pt SAC was studied at the single-molecule single-atom level. Both static and dynamic activity heterogeneity are observed in Pt SAC. It reveals that the intrinsic catalytic activity of Pt SAC is higher than that of Pt nanoparticles (NPs), although they follow the same bimolecular competition mechanism. Significantly, Pt SAC presents no catalysis-induced surface restructuring, meaning that the dynamic activity fluctuation of Pt SAC can only be attributed to the spontaneous surface restructuring, and the catalysis process does not affect much of the structure of $Pt_1$-based active sites, all different from Pt NP catalysis, in which the surface restructuring and the catalysis can affect each other. Further, density functional theory (DFT) calculation indicates that the unique catalytic properties of Pt SAC or the different catalytic properties between Pt SAC and NPs could be attributed to the strong adsorptions of both reactant and product on Pt SAC, large surface energy of Pt SAC, and strong binding of $Pt_1$ on support. Knowledge revealed here provides fundamental insights into the catalysis of atomically dispersed catalyst.**

single-molecule fluorescence microscopy | single-atom catalysis | catalytic kinetics and dynamics | individual atom | surface restructuring

## Significance

Here, with single-molecule fluorescence microscopy, we study the catalytic behavior of individual Pt atoms at single-turnover resolution, and then reveal the unique catalytic properties of Pt single-atom catalyst and the difference in catalytic properties between individual Pt atoms and Pt nanoparticles. Further density functional theory calculation indicates that unique catalytic properties of Pt single-atom catalyst could be attributed intrinsically to the unique surface properties of $Pt_1$-based active sites.

Atomically dispersed metals or metal single-atom catalysts (SACs) have recently attracted a large amount of attention due to their extremely high atom efficiency or metal utilization (~100%) (1–4). For precious metals, such as Pt (3, 5, 6), Au (7, 8), Pd (9–11), and Ir (12, 13), their SACs as the most cost-effective catalysts are very desirable for practical applications.

For metal SACs, the individual metal atoms are anchored tightly on supports (such as carbon materials, metals, or metal oxides) via a strong interaction between individual metal atoms and supports (6, 10, 14, 15). Such strong anchoring usually occurs via the vacancy or defects on supports (5, 11, 13, 16). The catalytic activity or selectivity of a SAC usually depends strongly on the choice of support (3, 17–21), which directly determines the structure of the single-metal atom–based active sites. To deeply understand the unique catalytic properties of SACs and reveal the property differences between traditional metal nanoparticle (NP)-based catalysts and SAC (6, 9, 13, 15, 22–24), here, based on single-molecule fluorescence microscopy (SMFM) (25–29), we study the nanocatalysis of Ceria ($CeO_2$)-supported (30) Pt SAC for a fluoregenic reaction (31, 32) at the single-molecule single-atom level in real time with single-turnover resolution. It reveals both static and dynamic activity heterogeneity in the catalysis of Pt SAC. Significantly, no catalysis-induced surface restructuring can be observed on Pt SAC, which means that the dynamic activity fluctuation of Pt SAC can only be attributed to the spontaneous surface restructuring, and the catalysis process does not affect the surface restructuring of Pt SAC on $CeO_2$. Further, density functional theory (DFT) calculation indicates that the observed unique catalytic properties of Pt SAC and the difference of catalytic properties between Pt SAC and NPs could be attributed to the stronger adsorptions of both reactant and product on Pt SAC, larger surface energy of Pt SAC, and stronger binding of $Pt_1$ on $CeO_2$ than those on Pt NPs. Such results deepen our understanding of the intrinsic catalytic properties of SAC and may help in the design of highly efficient SACs.

## Results and Discussion

**Synthesis and Characterization of Atomically Dispersed $Pt_1$@$CeO_2$.** $CeO_2$ nanocrystals, the support of Pt SACs adopted here, were synthesized based on literature (33), with $Ce(NO_3)_3$ as precursor via hydrothermal treatment at 160 °C and then pyrolysis at 1,000 °C sequentially. As shown in Fig. 1 *A* and *B*, the obtained $CeO_2$ nanocrystals with an average size of about 112 ± 6 nm could be dispersed individually without aggregation. After the sparse deposition of individual Pt atoms on $CeO_2$ nanocrystals

Author affiliations: [a]State Key Laboratory of Electroanalytical Chemistry, Changchun Institute of Applied Chemistry, Chinese Academy of Sciences, Changchun 130022, People's Republic of China; [b]Jilin Province Key Laboratory of Low Carbon Chemical Power, Changchun Institute of Applied Chemistry, Chinese Academy of Sciences, Changchun 130022, People's Republic of China; [c]University of Science and Technology of China, Anhui 230026, China; [d]Wenzhou Institute, University of Chinese Academy of Sciences, Wenzhou 352001, China; [e]Key Laboratory of Automobile Materials MOE (Ministry of Education), Jilin University, Changchun 130012, China; [f]School of Materials Science & Engineering, Jilin University, Changchun 130012, China; [g]Jilin Provincial International Cooperation Key Laboratory of High-Efficiency Clean Energy Materials, Jilin University, Changchun 130012, China; [h]Electron Microscopy Center, Jilin University, Changchun 130012, China; and [i]International Center of Future Science, Jilin University, Changchun 130012, China

Author contributions: X.L. and W.X. designed research; X.L. and J.C. performed research; X.G., J.C., Y.W., W.Z., and P.S. contributed new reagents/analytic tools; X.L., X.G., J.C., Y.X., W.Z., and P.S. analyzed data; and X.L., P.S., and W.X. wrote the paper.

The authors declare no competing interest.

This article is a PNAS Direct Submission.



[1]X.L., X.G., and J.C. contributed equally to this work.

[2]To whom correspondence may be addressed. Email: weizhang@jlu.edu.cn, songping@ciac.ac.cn, or weilinxu@ciac.ac.cn.

This article contains supporting information online at http://www.pnas.org/lookup/suppl/doi:10.1073/pnas.2114639119/-/DCSupplemental.

Published March 29, 2022.

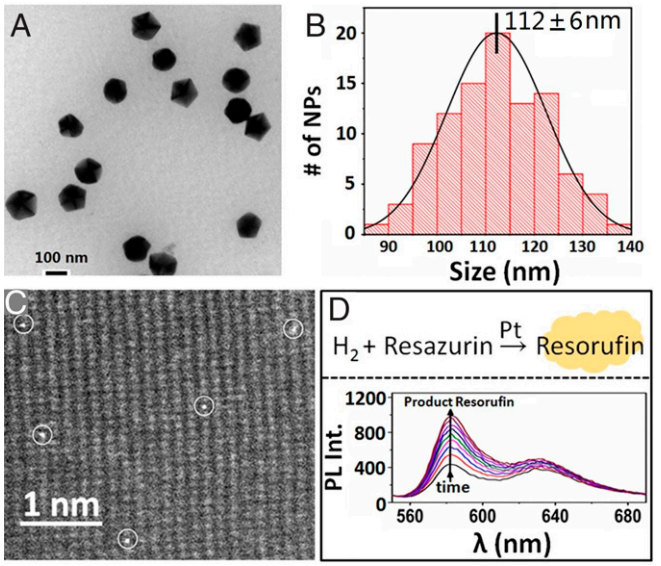


**Fig. 1.** Characterization of atomically dispersed $Pt_1@CeO_2$. (*A*) Typical TEM image of $CeO_2$ nanocrystals as support for Pt SACs. (*B*) Size statistical analysis of $CeO_2$ nanocrystals. (*C*) Typical HAADF-STEM image of the $Pt_1@CeO_2$ catalyst (with Pt 0.05 wt %) to show the dispersion of individual Pt atoms on surface of $CeO_2$. (*D*) (*Top*) The Pt catalyzed reduction reaction of resazurin by hydrogen to produce fluorescent product resorufin; (*Bottom*) the in situ fluorescence spectra of the $Pt_1@CeO_2$(0.05 wt % of Pt)-catalyzed reduction reaction of resazurin by $H_2$ to produce highly fluorescent resorufin in aqueous solution ($\lambda_{ex}$ = 532 nm). The arrow indicates the gradual formation of product resorufin with time.

(*SI Appendix*), the obtained sample, named as $Pt_1@CeO_2$, was characterized by high-angle annular dark-field scanning transmission electron micros (HAADF-STEM) to monitor the dispersion of Pt atoms on $CeO_2$ support. Typically, for the sample of $Pt_1@CeO_2$ with Pt loading of 0.05 wt.% (Fig. 1*C*), as expected, the individual Pt atoms are dispersed sparsely on the surface of $CeO_2$ nanocrystals. To study the catalytic activity of $Pt_1@CeO_2$, the Pt-catalyzed fluoregenic reaction (the reduction reaction of nonfluorescent resazurin to highly fluorescent resorufin by $H_2$; Fig. 1*D*) was adopted as the model reaction (31, 32). The control experiment shows that the pure $CeO_2$ nanocrystals are inert to such reaction (*SI Appendix*, Fig. S1); only with the addition of $Pt_1@CeO_2$, the reduction reaction of resazurin by hydrogen can occur rapidly as indicated by the time-dependent increase of fluorescence signal of the product resorufin at 583 nm (Fig. 1*D* and *SI Appendix*, Fig. S1), confirming that the individual Pt atoms ($Pt_1@CeO_2$), just like traditional Pt NPs (31), indeed, can effectively catalyze such fluoregenic reduction reaction.

The single-molecule nanocatalysis of $Pt_1@CeO_2$ was then done based on the above fluorogenic reaction. To study the nanocatalysis of such Pt SAC at the single-molecule single-atom level, based on the mass density (1.9 g/mL) of obtained powder of $CeO_2$ nanocrystals with an average size of 112 nm (Fig. 1 *A* and *B*), a $Pt_1@CeO_2$ catalyst with an extremely low Pt loading of 0.00001 wt.% (or 0.1 ppm) (*SI Appendix*, Scheme S1) was synthesized for the fluoregenic reaction to make sure that the averaged number ($n$) of Pt atoms on a single $CeO_2$ NP is much smaller than one ($n < 1$). It means, for such $Pt_1@CeO_2$, there is statistically only one or zero Pt atoms on the surface of a single $CeO_2$ nanocrystal. By sparsely dispersing such individual $CeO_2$ NPs with one or zero Pt atoms on a quartz slide surface (*SI Appendix*, Fig. S2), one can make sure that the fluorescence signal obtained from each location is from the product molecules formed on a single Pt atom sitting on a $CeO_2$ nanocrystal (Fig. 2*A*). Such single-molecule nanocatalysis was conducted in a microfluidic channel, as shown in Fig. 2*B*. By flowing the solution containing both nonfluorescent resazurin and saturated hydrogen into the channel, the reduction of resazurin by hydrogen was then catalyzed by $Pt_1@CeO_2$ to produce rapidly fluorescent product resorufin, which was then excited by a green (532 nm) laser to produce fluorescence and detected via an electron-multiplying charge coupled device (EMCCD) camera at an operating rate of 100 ms per frame. The stochastic fluorescence bursts at many localized spots with individual $Pt_1@CeO_2$ were recorded in movies by total internal reflection fluorescence (TIRF) microscope (34, 35); each spot gives out a stochastic trajectory with fluorescence bursts (Fig. 2*C*) to indicate the in situ catalysis process occurring on a single Pt atom–based active site (26). Each fluorescence burst could be attributed to the formation and the subsequent dissociation of a fluorescent product resorufin molecule on a single Pt atom–based active site. The observed stochastic fluorescence off–on signal on turnover trajectory of fluorescence contains two waiting times, $\tau_{off}$ and $\tau_{on}$ (Fig. 2*C*), by dividing a catalytic cycle into two parts. $\tau_{off}$ is the waiting time before the formation of a product molecule; $\tau_{on}$ represents the time that one product molecule spends before it dissociates from catalyst surface (26).

**The Catalytic Kinetics of Atomically Dispersed $Pt_1@CeO_2$.** It has been known that the above $\tau_{off}$ contains the kinetic information of the catalytic product formation process, and $\tau_{on}$ contains that of product dissociation process (26). Therefore, the whole catalytic kinetics on a single Pt atom can be probed by resolving these two waiting times. Here, the reaction kinetics can be defined by the statistical properties. The statistical properties of $<\tau_{off}>^{-1}$ and $<\tau_{on}>^{-1}$ obtained from a single trajectory represent the time-averaged product formation rate and product desorption rate on a Pt atom, respectively (26). When averaging the turnover trajectories from many individual Pt atoms, the relationship between reaction rate and substrate concentrations can be obtained reliably.

Interestingly, as shown in Fig. 3*A*, in the $H_2$-saturated ($[H_2]$ = 0.8 mM) solution, the average product formation rate ($<\tau_{off}>^{-1}$) on a single Pt atom initially increases with substrate resazurin concentration and then decreases inversely after a maximum, similar to the catalytic product formation process on a single Pt NP for the same reaction (*SI Appendix*, Fig. S3*A*) (31). Obviously, such decay of the product formation rate at high substrate concentration could be attributed to the bimolecular competition mechanism between two different substrate molecules (resazurin and hydrogen) (25, 29) rather than the deactivation (*SI Appendix*, Fig. S4). Moreover, as shown in *SI Appendix*, Fig. S5, at the same substrate concentration and reaction temperature (298 K), the product formation rates obtained here on a single Pt atom ($Pt_1@CeO_2$) are all smaller than that on a single Pt NP with an average size of 4.9 nm (31), mainly due to the fact that the product formation rate on a single Pt NP is the sum of the product formation rates of multiple Pt active sites on the surface of a Pt NP. As for the product desorption process on a single $Pt_1@CeO_2$, Fig. 3*B* shows that the product dissociation rate ($<\tau_{on}>^{-1}$) is independent of the substrate concentration, which is also the same as that observed from traditional single Pt NP for the same product dissociation process (*SI Appendix*, Fig. S3*B*) (31).

The above analysis indicates that the total catalytic reaction follows the bimolecular reaction mechanism (25, 29), as shown in Fig. 3*C*, in which the substrate and product molecules maintain fast adsorption/desorption equilibrium on the catalyst.

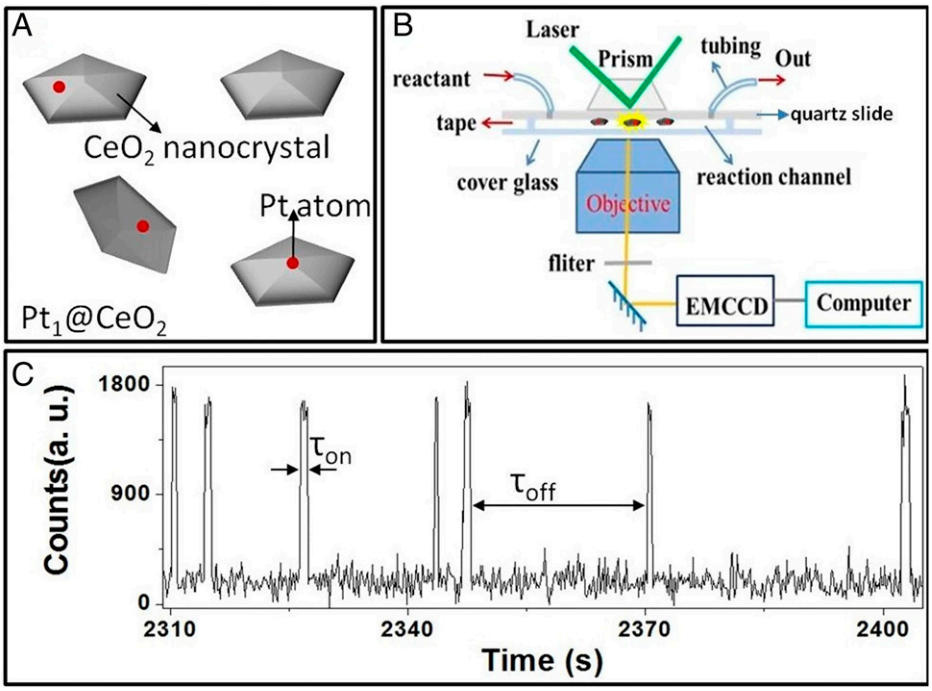


**Fig. 2.** Scheme of $Pt_1@CeO_2$ and single-molecule nanocatalysis. (*A*) Scheme to show that the number of Pt atoms on a single $CeO_2$ nanocrystal is one or zero for $Pt_1@CeO_2$ with Pt loading of 0.1 ppm. (*B*) Experimental optical setup for TIRF microscopy and the single-molecule nanocatalysis in a microflow cell based on the reduction reaction of resazurin by $H_2$ to produce resorufin catalyzed by atomically dispersed $Pt_1@CeO_2$. (*C*) Typical fluorescence intensity turnover trajectory of a single atomically dispersed $Pt_1@CeO_2$ in $H_2$-saturated resazurin (10 nM) solution at 100-ms time resolution.

Based on previous knowledge, the product formation rate per particle can be expressed as (26)

$$\langle \tau_{off} \rangle^{-1} = \frac{\gamma_{eff} \alpha_A [A] \alpha_B [\mathrm{B}]}{(1 + \alpha_A [A] + \alpha_B [B])^2}, \quad [1]$$

and the product dissociation rate is

$$\langle \tau_{on} \rangle^{-1} = \frac{\gamma_2 G[\mathrm{B}] + \gamma_3}{1 + G[B]}. \quad [2]$$

Here, $[A]$ and $[B]$ represent the concentrations of $H_2$ and resazurin, respectively; $\gamma_{eff} (= \gamma n_T)$ is the effective rate constant for the catalytic product formation process on a single particle (Fig. 3*C*); $\gamma$ is the effective rate constant per active site; $n_T$ is the total number of active site on a single particle; $\alpha_A$ and $\alpha_B$ are the adsorption equilibrium constants of $H_2$ and resazurin; $\gamma_2$ and $\gamma_3$ are the rate constants for the indirect and direct dissociation process of product; and $G\left(= \gamma_1 [A]/(\gamma_{-1} + \gamma_2)\right)$. For this case, since there is only one or zero atom on a single $CeO_2$ NP ($Pt_1@CeO_2$), then, here, $n_T = 1$, so $\gamma_{eff} = \gamma$.

By fitting the experimental data of the product formation rates and dissociation rates using the above equations (Fig. 3 *A* and *B*), the corresponding kinetic parameters for the product formation process ($\gamma_{eff}$ or $\gamma$, $\alpha_A$, and $\alpha_B$) and product direct dissociation process ($\gamma_3$) were obtained as shown in Table 1. To reveal the difference of the catalytic properties between single Pt atoms and single Pt NPs, the kinetic parameters obtained before for single Pt NPs (~4.9 nm) (31) for the same reduction reaction are also listed in Table 1 for comparison. It clearly shows that the effective rate constant $\gamma_{eff}$ per Pt NO is about 4 times that per Pt atom obtained here, mainly due to the fact that the number of active sites ($n_T$) on a single Pt NP is much larger than one (Table 1). While, due to the fact that the value of $n_T$ on a single Pt NP (~4.9 nm) is much larger than one or five, one can expect that the value of "apparent" $\gamma$ ($= \gamma_{eff}/n_T$) per active site on Pt NP is smaller than that per active site on Pt SAC ($Pt_1@CeO_2$), such a difference could be mainly attributed to the different structure of active sites and the steric hindrance effect induced by the crowding of active sites on the surface of traditional Pt NPs (*SI Appendix*, Fig. S6); it is also part of the reason for the higher atom efficiency or metal utilization of SAC than traditional metal NPs. As for the adsorption ability of substrate molecules, as shown in Table 1, $H_2$ adsorption on $Pt_1@CeO_2$ is stronger than that on Pt NPs, while the resazurin adsorption on $Pt_1@CeO_2$ shows no big difference from that on Pt NPs; as for the desorption of product resorufin, $\gamma_3$ in Table 1 shows that the direct dissociation pathway on Pt NPs is faster than that on $Pt_1@CeO_2$, indicating that the adsorption of product resorufin on $Pt_1@CeO_2$ is stronger than that on Pt NPs.

**The Static Heterogeneity of Catalytic Activity of Atomically Dispersed $Pt_1@CeO_2$.** In order to further quantify the difference of catalytic activity of individual atomically dispersed $Pt_1@CeO_2$, the probability density function $f_{off}(\tau)$ (26, 36) of $\tau_{off}$ for product formation process was adopted to evaluate the static heterogeneity of the catalytic activity among different single Pt atoms,

$$f_{off}(\tau) = \gamma_{app} exp(-\gamma_{app} \tau). \quad [3]$$

Here, $\gamma_{app}$ is the apparent catalytic rate constant for product formation process on a single Pt atom ($Pt_1@CeO_2$). As shown in Fig. 3*D*, a typical distribution of $\tau_{off}$ from one turnover trajectory was fitted with Eq. **3** to obtain the value of apparent catalytic rate constant $\gamma_{app}$ of a single Pt atom on $CeO_2$. Fig. 3*E* shows the distribution of $\gamma_{app}$ from multiple individual Pt atoms. The broad distribution of $\gamma_{app}$, corresponding to a large value (90%) of the heterogeneity index (defined as the full width at half maximum/$(\ln 4)^{1/2}$ [full width at half maximum from the Gaussian distribution] divided by the average ($<\gamma_{app}>$)) (31), indicates a huge static activity heterogeneity among different individual Pt atoms. Such static heterogeneity

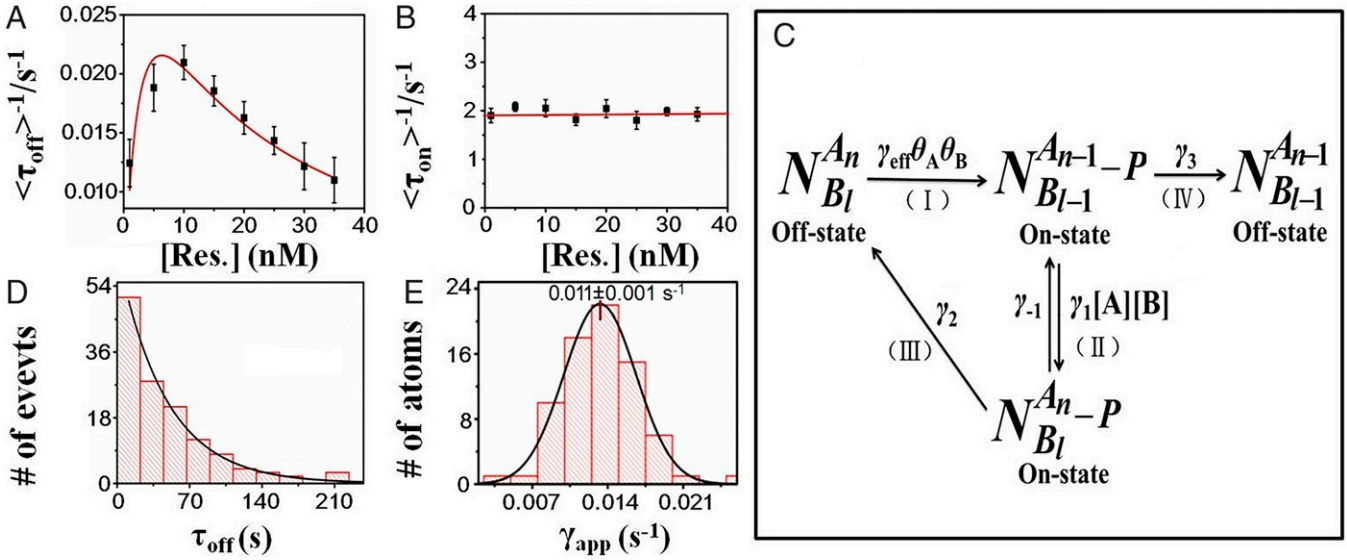


**Fig. 3.** Catalytic kinetics of atomically dispersed $Pt_1@CeO_2$. (*A* and *B*) Single-molecule catalytic kinetics of atomically dispersed $Pt_1@CeO_2$. In $H_2$-saturated solution, the product formation rate ($<\tau_{off}>^{-1}$) (*A*) is dependent on resazurin concentration, and the product desorption rate ($<\tau_{on}>^{-1}$) (*B*) is independent of it. Each datum is obtained from the average of more than 80 individual turnover trajectories or particles, with the error bar showing SE. Solid lines are fitted with Eq. **1** with $\gamma_{eff} = 0.12\ s^{-1}$, $\alpha_A = 1.07\ mM^{-1}$, and $\alpha_B = 0.32\ nM^{-1}$. (*C*) Kinetic mechanism of the reduction reaction catalyzed by Pt NP, including the product formation and dissociation process. The meaning of each symbol is described in detail in the *SI Appendix*. (*D*) $\tau_{off}$ distribution from a single trajectory of atomically dispersed $Pt_1@CeO_2$ with [resazurin] = 30 nM in $H_2$-saturated solution; it is fitted by a single exponential with the constant $\gamma_{app} = 0.011 \pm 0.001\ s^{-1}$. (*E*) The distribution of $\gamma_{app}$ from multiple trajectories or individual atomically dispersed $Pt_1@CeO_2$; solid line is Gaussian fit.

could be attributed to the different microenvironments among different individual Pt atoms mainly induced by the support of $CeO_2$ nanocrystals, such as the different facets with different oxygen vacancies or defects for the anchoring of individual Pt atoms (37–39).

**The Catalytic Dynamics of Atomically Dispersed $Pt_1@CeO_2$.** To further study the catalytic dynamics of individual atomically dispersed $Pt_1@CeO_2$, we determined the activity fluctuations of multiple individual atomically dispersed $Pt_1@CeO_2$. The activity fluctuations are reflected by the variation of reaction rates in both the product formation process ($\tau_{off}$) and product dissociation process ($\tau_{on}$). Here, to analyze the activity fluctuations of individual Pt atoms on $CeO_2$, the individual $\tau_{off}$ and $\tau_{on}$ were extracted from multiple individual turnover trajectories, and then calculated with the autocorrelation function $C_\tau(m) = \langle \Delta\tau(0)\Delta\tau(m)\rangle / \langle \Delta\tau^2 \rangle$ (26). Here, $\tau$ represents $\tau_{off}$ or $\tau_{on}$, $m$ is the turnover index number from the sequence, and $\Delta\tau(m) = \tau(m) - \langle\tau\rangle$. If $Pt_1@CeO_2$ possesses catalytic dynamic heterogeneity, $C_\tau(m)$ will be positive and show a decay behavior with a decay time constant; such a time constant is the activity fluctuation correlation time (26).

As shown in Fig. 4 *A* and *B*, both the typical $C_{\tau off}$ and $C_{\tau on}$ present an exponential decay tendency, indicating the existence of activity fluctuations in the catalytic product formation ($\tau_{off}$) and dissociation process ($\tau_{on}$), respectively, occurring on the active sites of single $Pt_1@CeO_2$. For the single-atom Pt corresponding to the data shown in Fig. 4 *A* and *B*, the decay constants of $C_\tau$ at a certain substrate concentration are $m_{off} = 1.9 \pm 0.5$ turnovers and $m_{on} = 1.2 \pm 0.4$ turnovers. Based on the average turnover time (83 s) of this turnover trajectory, the fluctuation correlation times for the $\tau_{off}$ and $\tau_{on}$ reactions are ~159 and 96 s, respectively. Here, the fluctuation timescales of the dynamic surface restructuring can be reflected by these two correlation times (26). Moreover, the activity fluctuations could be attributed to the small-scale dynamic conformation restructuring or distortion. That is to say that the correlation times of fluctuation activity are the timescales of the surface restructuring dynamics. For an SAC of $Pt_1@CeO_2$, the activity fluctuation of individual atomically dispersed $Pt_1@CeO_2$ could be attributed to small-scale dynamic conformation restructuring or distortion around the individual active sites, similar to that of NPs (26, 27). Here, the distributions (Fig. 4 *A* and *B*, *Insets*) of the fluctuation correlation times of atomically dispersed $Pt_1@CeO_2$ are wide (the width of the time distribution is about 200 s), probably due to the different microenvironment around each $Pt_1@CeO_2$, resulting in the diverse interaction between Pt atoms and support $CeO_2$.

To further reveal the relevance between activity fluctuations and surface restructuring, we plotted the activity fluctuation rates ($v_{off} = v_{spon\text{-}off} + v_{cata\text{-}off}$, $v_{on} = v_{spon\text{-}on} + v_{cata\text{-}on}$; $v_{spon}$ is the spontaneous fluctuation rate, and $v_{cata}$ is the catalysis-induced fluctuation rate) against the turnover rates at various reactant concentrations for both $\tau_{off}$ and $\tau_{on}$ processes (26). Here, the fluctuation rates are the inverses of the correlation times. As shown in Fig. 4*C*, for atomically dispersed $Pt_1@CeO_2$, the activity fluctuation rates for both the $\tau_{off}$ reaction and the $\tau_{on}$ reaction are

**Table 1. Comparison of the catalytic kinetics and dynamics between Pt SAC and Pt NPs (31)**

| | $n_T$ | $<\gamma_{eff}>$ ($s^{-1}$) | $<\gamma>$ ($s^{-1}$) | $\alpha_A$ ($mM^{-1}$) | $\alpha_B$ ($nM^{-1}$) | $<\gamma_3>$ ($s^{-1}$) | $v_{spon\text{-}off}$ ($s^{-1}$) | $v_{spon\text{-}on}$ ($s^{-1}$) |
|---|---|---|---|---|---|---|---|---|
| Pt NPs | >>1 | 0.51 ± 0.12 | ($0.51/n_T$) <<0.12 | 0.31 ± 0.20 | 0.28 ± 0.15 | 2.35 ± 0.02 | 0.003 ± 0.001 | 0.002 ± 0.001 |
| $Pt_1@CeO_2$ | 1 | 0.12 ± 0.02 | 0.12 | 1.07 ± 0.10 | 0.32 ± 0.05 | 1.91 ± 0.10 | 0.007 ± 0.001 | 0.011 ± 0.002 |

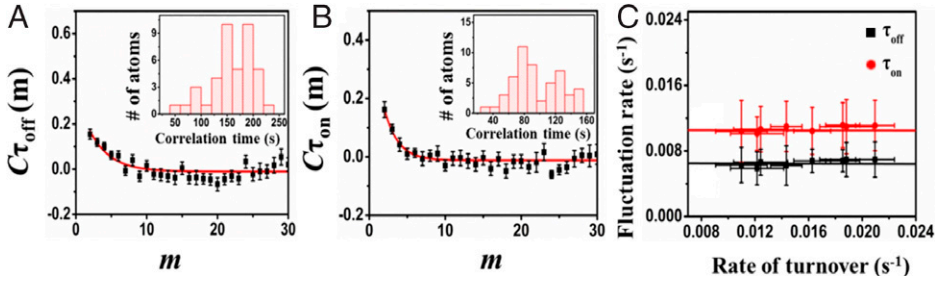


**Fig. 4.** (*A* and *B*) Exemplary autocorrelation function $C_\tau(t)$ of $\tau_{off}$ (*A*) and $\tau_{on}$ (*B*) from turnover trajectories of individual atomically dispersed $Pt_1@CeO_2$ at 35 nM resazurin. The *x* axis is the turnover index. The solid line is the fit with a single exponential for decay constants of $m_{off}$ = 1.9 ± 0.5 turnovers and $m_{on}$ = 1.2 ± 0.4 turnovers. (*Insets*) The distribution of the fluctuation time for $\tau_{off}$ and $\tau_{on}$ processes, respectively. (*C*) Dependences of the rates of activity fluctuation (the inverse of fluctuation correlation time) of $\tau_{off}$ and $\tau_{on}$ processes on the turnover rates. Each data point is an average from >80 trajectories here. Error bars are SE.

almost independent of the turnover rates (Fig. 4*C*), indicating that the fluctuation rate does not change with the substrate concentration, and the values of both $v_{cata\text{-}off}$ and $v_{cata\text{-}on}$ are zero at any substrate concentration. The substrate concentration–independent activity fluctuation observed here on Pt SCA reflects that the underlying dynamic conformation restructuring existing among atomically dispersed $Pt_1@CeO_2$ is mainly due to the spontaneous surface restructuring of the single-atom Pt–based active site ($Pt_1@CeO_2$) (26); the catalytic process or the substrate binding/product unbinding approximately has no effect on structure of the Pt SAC-based active sites. As for the Pt NPs, interestingly, as shown in *SI Appendix*, Fig. S7 and reported before (31), the catalytic process or the substrate binding/product unbinding can affect hugely the surface restructuring of the Pt NP surface, which is also called "catalysis-induced surface restructuring." Such a huge difference between Pt SAC and the Pt NPs revealed here probably indicates that the binding of $Pt_1$ to $CeO_2$ is much stronger than the binding of $Pt_1$ to $Pt_n$, or the structure of $Pt_1$–$CeO_2$ is much more stable than that of $Pt_1$–$Pt_n$. Furthermore, as shown in Fig. 4*C* and Table 1, the rate of spontaneous surface restructuring can be obtained ($v_{spon\text{-}off}$ =0.007 ± 0.001 $s^{-1}$ for the product formation process [$\tau_{off}$] and $v_{spon\text{-}on}$ =0.011 ± 0.002 $s^{-1}$ for product desorption [$\tau_{on}$] process), corresponding to a timescale of about 90 s to 160 s of the spontaneous surface reconstruction. The revealing of two different rates of spontaneous surface restructuring indicates that there are at least two different models of spontaneous surface restructuring on the same surface; the slow one (0.007 ± 0.001 $s^{-1}$) can affect the product formation process or the substrate binding, and the faster one (0.011 ± 0.002 $s^{-1}$) can affect the product dissociation process or the product unbinding. Interestingly, as shown in Table 1, for both the product formation and dissociation process on Pt NPs, the rates of spontaneous surface restructuring are smaller than that on Pt SAC ($Pt_1@CeO_2$), indicating that the structure of the individual Pt active site on Pt NP is much more stable than that of the single Pt atom–based active site on $CeO_2$ surface, and the reactant binding/product unbinding can activate the surface of Pt NPs and speed up or enhance its surface restructuring.

Furthermore, we did a DFT calculation to deeply understand the above observation about the unique properties of Pt SAC and the property differences between Pt SAC and Pt NPs($Pt_n$) shown above in Table 1. Based on the HAADF-STEM image (Fig. 1*C*) of $Pt_1@CeO_2$ and previous reports about the structure of $Pt_1@CeO_2$ (33, 38), DFT calculations about $Pt_1@CeO_2$ were done here based on a model with individual Pt atoms trapped by surface Ce vacancies on $CeO_2$ crystals (Fig. 5 and *SI Appendix*, Table S1). Firstly, we calculated the adsorption energies ($E_{ad}$) of both reactants and products on different surfaces. For the case with the coexistence of one $H_2$ molecule and one resazurin molecule around the active site (*SI Appendix*, Fig. S8*A*) (40), results in Fig. 5 show clearly that adsorption energies ($E_{ad}$) of both $H_2$ ($E_{ad1H\text{-}H2}$ = −0.517 eV) and resazurin ($E_{ad1H\text{-}R}$ = −0.382 eV) on $Pt_1@CeO_2$ are larger than those ($E_{ad1H\text{-}H2}$ = −0.420 eV; $E_{ad1H\text{-}R}$ = −0.314 eV) on $Pt_n$, indicating stronger adsorptions of both $H_2$ and resazurin on $Pt_1@CeO_2$ than on $Pt_n$, consistent with the obtained values of $\alpha_A$ and $\alpha_B$ shown in Table 1. As for the adsorption of product resorufin, its $E_{ad}$ on $Pt_1@CeO_2$ (−0.228 eV) is also larger than that (−0.204 eV) on $Pt_n$, indicating a stronger adsorption of resorufin on $Pt_1@CeO_2$ than on $Pt_n$, further confirming the slower dissociation (smaller $\gamma_3$) of product resorufin from $Pt_1@CeO_2$ than that from $Pt_n$ shown in Table 1. To understand the bimolecular competition mechanism for this redox reaction catalyzed by both $Pt_1@CeO_2$ and Pt NPs (Fig. 3*C* and *SI Appendix*, Fig. S5), we further calculated $E_{ad}$ of reactants ($H_2$ and resazurin) by increasing the number of $H_2$ molecules or [$H_2$] around the active sites (41, 42). For the case with the coexistence of four $H_2$ molecules and one resazurin molecule around the active site (*SI Appendix*, Fig. S8*B*), Fig. 5 shows the variations of $E_{ad}$ with the increase of [$H_2$]: For the adsorption on $Pt_1/CeO_2$, the adsorption energy of $H_2$ increases about 17%, while the adsorption energy of resazurin decreases 15% inversely; as for the adsorption on Pt NPs, the adsorption energy of $H_2$ decreases 57%, while the adsorption energy of resazurin increases inversely about 50%. Obviously, all these results confirm the

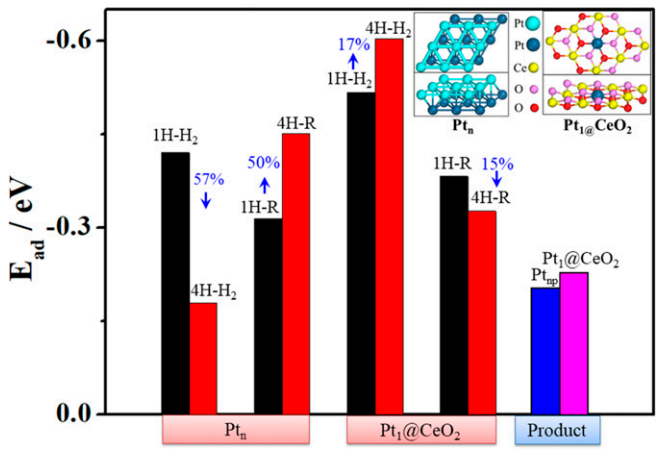


**Fig. 5.** Adsorption energies ($E_{ad}$) of $H_2$, resazurin (R) and product resorufin (Product) on different surfaces ($Pt_n$, $Pt_1@CeO_2$). *Insert* shows local structures of Pt(111) surface on Pt NPs ($Pt_n$) and $Pt_1@CeO_2$(111). The 1H and 4H represent the cases with one and four $H_2$ molecules around different surfaces, respectively.

**Table 2. Comparison of surface energy ($E_{surf}$), binding energy ($E_b$), and effect of the surface reconstruction on catalysis between Pt NPs and $Pt_1@CeO_2$**

| | $E_{surf}$ (eV/Å$^2$) | $E_b$ (eV) | Effect between catalytic process and surface reconstruction of different surfaces |
|---|---|---|---|
| Pt NPs | 0.09 | −6.972 | Catalytic process ⇌ surface reconstruction |
| $Pt_1@CeO_2$ | 0.19 | −12.560 | Catalytic process ⇌ surface reconstruction |

bimolecular competition mechanism observed on both $Pt_1@CeO_2$ and Pt NPs.

Moreover, we also found that the surface energy ($E_{surf}$; Table 2) of $Pt_1@CeO_2$ (0.190 eV/Å$^2$, in *SI Appendix*) is larger than that (0.090 eV/Å$^2$) of $Pt_n$, confirming the observed higher activity ($\gamma$) and faster spontaneous surface restructurings ($\upsilon_{spon\text{-}off}$ and $\upsilon_{spon\text{-}on}$) of $Pt_1@CeO_2$ than that of Pt NPs (Table 1) (43). Further results (Table 2) show that the binding of a Pt single atom on substrate $CeO_2$ ($E_b$ = −12.560 eV) is much stronger than that ($E_b$ = −6.972 eV) on Pt NPs, explaining the above observations on $Pt_1@CeO_2$ without catalysis-induced surface restructuring (Fig. 4*C*) and the observations on Pt NPs with catalysis-induced surface restructuring (*SI Appendix*, Fig. S7) (31). To further confirm such difference, HAADF-STEM was adopted to analyze the possible effect of the catalysis process on the microstructure of the active sites on both $Pt_1@CeO_2$ and Pt NPs. As shown in *SI Appendix*, Fig. S9 *A* and *B*, after a long-term (10 h) catalytic process for the fluoregenic reaction shown in Fig. 1*D*, the microstructures of $Pt_1$-based active sites on $CeO_2$ show almost no variation; such a fact indicates that the restructuring during catalysis is too gentle to much affect the structure of a $Pt_1$-based active site on $CeO_2$, confirming that the underlying dynamic conformation restructuring existing among atomically dispersed $Pt_1@CeO_2$ is mainly due to the spontaneous surface restructuring of the single-atom Pt–based active site ($Pt_1@CeO_2$), while the surface structure of traditional Pt NPs shows tremendous variation after the same catalytic process as shown in *SI Appendix*, Fig. S9 *C* and *D*, indicating that the catalysis process on Pt NPs is relatively violent and then leads to serious surface restructuring. Such facts confirm the above catalytic property differences between $Pt_1@CeO_2$ and Pt NPs. Significantly, the stronger binding (large $E_b$) of the Pt atom on $CeO_2$ and the faster spontaneous restructuring of $Pt_1@CeO_2$ than Pt NPs indicate that the spontaneous surface restructuring observed on $Pt_1@CeO_2$ mainly originates from the surface restructuring of $CeO_2$ around the $Pt_1$ center; it also implies that the reactants/products adsorption/desorption or catalysis process can intensify the restructuring amplitude of a surface with a slow spontaneous restructuring, while, if the initial spontaneous restructuring of a surface is fast enough, then the reactants/
products adsorption/desorption or catalysis process cannot much affect its surface restructuring. So, as shown in Table 2, for Pt NPs, the catalytic process and surface reconstruction can affect each other, like the previous observation on Au NPs (26), while, for the unique SAC $Pt_1/CeO_2$ studied here, its surface reconstruction can affect the catalytic process; inversely, the catalytic process cannot affect its surface reconstruction. In other words, the fast spontaneous reconstruction of a surface can weaken the effect from its environment.

## Discussion

In summary, the catalytic behavior of Pt SAC on $CeO_2$ ($Pt_1@CeO_2$) was studied via SMFM at the single-molecule single-atom level. Both static and dynamic activity heterogeneity were observed in the catalysis of $Pt_1@CeO_2$. It was found that Pt SAC follows the same bimolecular competition mechanism as Pt NP does for the same catalytic reaction, while the intrinsic catalytic activity per active site on Pt SAC is much higher than that on Pt NPs. Significantly, it was also found that the dynamic activity fluctuation of Pt SAC can only be attributed to the spontaneous surface restructuring, and no catalysis-induced surface restructuring can be observed due to the fast spontaneous surface restructuring, indicating that the catalysis process does not much affect the surface restructuring around the $Pt_1$-based active site on $CeO_2$, different from Pt NP catalysis in which the surface restructuring and the catalysis can affect each other. Further DFT calculation indicates that all these unique catalytic properties of Pt SAC or the difference from Pt NPs could be attributed to the stronger adsorption of both reactant and product on $Pt_1@CeO_2$, larger surface energy of $Pt_1@CeO_2$, and stronger binding of $Pt_1$ on $CeO_2$ than those on Pt NPs. The knowledge revealed here provides fundamental insights into the catalytic behaviors of atomically dispersed catalyst.

## Experimental Section

**Materials and Methods.** Platinum(IV) chloride, Cerium(III) nitrate hexahydrate, Propionic acid, and Ethylene glycol. These chemicals were used as received without further purification. Ultrapure Millipore water (18.2 MΩ cm) was used as the solvent throughout. Reactant resazurin was purchased from Sigma-Aldrich.

***Synthesis of single-atom $Pt_1@CeO_2$ catalyst.*** The synthesis of SAC $Pt_1@CeO_2$ with different amount of Pt loading was based on literature (33), with $Ce(NO_3)_3$ and $PtCl_4$ as precursors via sequential hydrothermal treatment at 160 °C and pyrolysis at 1,000 °C. The specific reaction process is introduced in *SI Appendix*.

***Single-molecule experiments.*** Single-molecule fluorescence measurements were performed on a home-built prism-type TIRF microscope based on an Olympus IX71 inverted microscope (*SI Appendix*). A continuous wave circularly polarized 532-nm laser beam was focused onto a small region on the sample. Then the fluorescence signal of the product was collected by a water immersion objective, and projected onto a camera controlled by Andor IQ software. The home-written interactive data language program was used to analyze the movies, which allows us to extract a time trajectory of fluorescence intensity from individual fluorescence spots on the sample.

**Data Availability.** All study data are included in the article and/or *SI Appendix*.

**ACKNOWLEDGMENTS.** This work was supported by the National Natural Science Foundation of China (grants 21925205, 22072145, 21733004, and 21721003), National Key R&D Program of China (grants 2017YFE9127900 and 2018YFB1502302) and K. C. Wong Education Foundation and Science.

1. P. Liu *et al.*, Photochemical route for synthesizing atomically dispersed palladium catalysts. *Science* **352**, 797–801 (2016).
2. J. Jones *et al.*, Thermally stable single-atom platinum-on-ceria catalysts via atom trapping. *Science* **353**, 150–154 (2016).
3. B. Qiao *et al.*, Single-atom catalysis of CO oxidation using $Pt_1/FeO_x$. *Nat. Chem.* **3**, 634–641 (2011).
4. X. Li *et al.*, Single-atom Pt as Co-catalyst for enhanced photocatalytic $H_2$ evolution. *Adv. Mater.* **28**, 2427–2431 (2016).
5. J. H. Kwak *et al.*, Coordinatively unsaturated $Al^{3+}$ centers as binding sites for active catalyst phases of platinum on $\gamma$-$Al_2O_3$. *Science* **325**, 1670–1673 (2009).
6. Y. Zhai *et al.*, Alkali-stabilized Pt-$OH_x$ species catalyze low-temperature water-gas shift reactions. *Science* **329**, 1633–1636 (2010).

7. A. Comas-Vives *et al.*, Single-site homogeneous and heterogeneized gold(III) hydrogenation catalysts: Mechanistic implications. *J. Am. Chem. Soc.* **128**, 4756–4765 (2006).
8. X. Zhang, H. Shi, B. Q. Xu, Catalysis by gold: Isolated surface $Au^{3+}$ ions are active sites for selective hydrogenation of 1,3-butadiene over $Au/ZrO_2$ catalysts. *Angew. Chem. Int. Ed. Engl.* **44**, 7132–7135 (2005).
9. S. Abbet *et al.*, Acetylene cyclotrimerization on supported size-selected $Pd_n$ clusters ($1 \leq n \leq 30$): One atom is enough! *J. Am. Chem. Soc.* **122**, 3453–3457 (2000).
10. G. Vilé *et al.*, A stable single-site palladium catalyst for hydrogenations. *Angew. Chem. Int. Ed. Engl.* **54**, 11265–11269 (2015).
11. H. Yan *et al.*, Single-atom $Pd_1$/graphene catalyst achieved by atomic layer deposition: Remarkable performance in selective hydrogenation of 1,3-butadiene. *J. Am. Chem. Soc.* **137**, 10484–10487 (2015).
12. J. Lin *et al.*, Remarkable performance of $Ir_1/FeO_x$ single-atom catalyst in water gas shift reaction. *J. Am. Chem. Soc.* **135**, 15314–15317 (2013).
13. V. Ortalan, A. Uzun, B. C. Gates, N. D. Browning, Direct imaging of single metal atoms and clusters in the pores of dealuminated HY zeolite. *Nat. Nanotechnol.* **5**, 506–510 (2010).
14. M. Yang *et al.*, Catalytically active $Au\text{-}O(OH)_x$-species stabilized by alkali ions on zeolites and mesoporous oxides. *Science* **346**, 1498–1501 (2014).
15. X. Yang, L. Yang, S. Lin, R. Zhou, New insight into the doping effect of $Pr_2O_3$ on the structure-activity relationship of $Pd/CeO_2$-$ZrO_2$ catalysts by Raman and XRD Rietveld analysis. *J. Phys. Chem. C* **119**, 6065–6074 (2015).
16. S. Sun *et al.*, Single-atom catalysis using Pt/graphene achieved through atomic layer deposition. *Sci. Rep.* **3**, 1775–1785 (2013).
17. X. Liu, O. Korotkikh, R. Farrauto, Selective catalytic oxidation of CO in $H_2$: Structural study of Fe oxide-promoted Pt/alumina catalyst. *Appl. Catal. A* **226**, 293–303 (2002).
18. D. Kalakkad, A. K. Datye, H. Robota, Interaction of platinum and ceria probed by transmission electron microscopy and catalytic reactivity. *Appl. Catal. B* **1**, 191–219 (1992).
19. S. H. Oh, P. Mitchell, R. Siewert, Methane oxidation over alumina-supported noble metal catalysts with and without cerium additives. *J. Catal.* **132**, 287–301 (1991).
20. J. M. Schwartz, L. D. Schmidt, Microstructures of Pt-Ce and Rh-Ce particles on alumina and silica. *J. Catal.* **138**, 283–293 (1992).
21. A. Abdel-Mageed, D. Widmann, S. Olesen, I. Chorkendorff, R. Behm, Selective CO methanation on highly active $Ru/TiO_2$ catalysts: Identifying the physical origin of the observed activation/deactivation and loss in selectivity. *ACS Catal.* **8**, 5399–5414 (2018).
22. W. E. Kaden, T. Wu, W. A. Kunkel, S. L. Anderson, Electronic structure controls reactivity of size-selected Pd clusters adsorbed on $TiO_2$ surfaces. *Science* **326**, 826–829 (2009).
23. H. Wei *et al.*, $FeO_x$-supported platinum single-atom and pseudo-single-atom catalysts for chemoselective hydrogenation of functionalized nitroarenes. *Nat. Commun.* **5**, 5634 (2014).
24. M. Yang *et al.*, A common single-site $Pt(II)\text{-}O(OH)_x$- species stabilized by sodium on "active" and "inert" supports catalyzes the water-gas shift reaction. *J. Am. Chem. Soc.* **137**, 3470–3473 (2015).
25. T. Chen *et al.*, Catalytic kinetics of different types of surface atoms on shaped Pd nanocrystals. *Angew. Chem. Int. Ed. Engl.* **55**, 1839–1843 (2016).
26. W. Xu, J. S. Kong, Y. T. Yeh, P. Chen, Single-molecule nanocatalysis reveals heterogeneous reaction pathways and catalytic dynamics. *Nat. Mater.* **7**, 992–996 (2008).
27. Y. Zhang *et al.*, Unique size-dependent nanocatalysis revealed at the single atomically precise gold cluster level. *Proc. Natl. Acad. Sci. U.S.A.* **115**, 10588–10593 (2018).
28. X. Zhou, W. Xu, G. Liu, D. Panda, P. Chen, Size-dependent catalytic activity and dynamics of gold nanoparticles at the single-molecule level. *J. Am. Chem. Soc.* **132**, 138–146 (2010).
29. X. Liu, T. Chen, P. Song, Y. Zhang, W. Xu, Single-molecule nanocatalysis of Pt nanoparticles. *J. Phys. Chem. C* **122**, 1746–1752 (2018).
30. Y. Nagai *et al.*, Sintering inhibition mechanism of platinum supported on ceria-based oxide and Pt-oxide-support interaction. *J. Catal.* **242**, 103–109 (2006).
31. X. Liu, T. Chen, W. Xu, Revealing the thermodynamics of individual catalytic steps based on temperature-dependent single-particle nanocatalysis. *Phys. Chem. Chem. Phys.* **21**, 21806–21813 (2019).
32. K. S. Han, G. Liu, X. Zhou, R. E. Medina, P. Chen, How does a single Pt nanocatalyst behave in two different reactions? A single-molecule study. *Nano Lett.* **12**, 1253–1259 (2012).
33. P. Xie *et al.*, Nanoceria-supported single-atom platinum catalysts for direct methane conversion. *ACS Catal.* **8**, 4044–4048 (2018).
34. Y. Zhang, P. Song, Q. Fu, M. Ruan, W. Xu, Single-molecule chemical reaction reveals molecular reaction kinetics and dynamics. *Nat. Commun.* **5**, 4238 (2014).
35. Y. Zhang *et al.*, Superresolution fluorescence mapping of single-nanoparticle catalysts reveals spatiotemporal variations in surface reactivity. *Proc. Natl. Acad. Sci. U.S.A.* **112**, 8959–8964 (2015).
36. W. Xu, H. Shen, G. Liu, P. Chen, Single-molecule kinetics of nanoparticle catalysis. *Nano Res.* **2**, 911–922 (2009).
37. L. Nie *et al.*, Activation of surface lattice oxygen in single-atom $Pt/CeO_2$ for low-temperature CO oxidation. *Science* **358**, 1419–1423 (2017).
38. X. Ye *et al.*, Insight of the stability and activity of platinum single atoms on ceria. *Nano Res.* **12**, 1401–1409 (2019).
39. Y. Tang, Y.-G. Wang, J. Li, Theoretical investigations of $Pt_1@CeO_2$ single-atom catalyst for CO oxidation. *J. Phys. Chem. C* **121**, 11281–11289 (2017).
40. L. Kuai *et al.*, Titania supported synergistic palladium single atoms and nanoparticles for room temperature ketone and aldehydes hydrogenation. *Nat. Commun.* **11**, 48 (2020).
41. W. Zhao *et al.*, Single $Mo_1(Cr_1)$ atom on nitrogen-doped graphene enables highly selective electroreduction of nitrogen into ammonia. *ACS Catal.* **9**, 3419–3425 (2019).
42. Y. Yang, Z. Zhao, R. Cui, H. Wu, D. Cheng, Structures, thermal stability, and chemical activity of crown-jewel-structured Pd–Pt nanoalloys. *J. Phys. Chem. C* **119**, 10888–10895 (2015).
43. H. Zhuang, A. J. Tkalych, E. A. Carter, Surface energy as a descriptor of catalytic activity. *J. Phys. Chem. C* **120**, 23698–23706 (2016).